Check for updates

Biomimetic Chemotactic Motion of Self-Assembling Doublet Microrobots

*Zuyao Xiao, Maximilian Voigtmann, and Juliane Simmchen**

Bio-hybrid robotics at the microscale promises to advance intelligent systems in biomedical devices, environmental monitoring, and soft robotics by emulating complex behaviors found in living entities, such as chemotaxis. Here, the shape-dependent chemotaxis of doublet microswimmers, with various morphologies that exhibit autonomous movement in hydrogen peroxide (H_2O_2) gradients without the need for complex material preparation, are reported. These microswimmers consist of a double-sphere structure composed of one colloid with a catalytic silver (Ag) surface and a second one with a passive silica surface. Catalytic decomposition of H_2O_2 on the Ag surface enables propulsion with the Ag side forward. In the presence of an H_2O_2 gradient, differential reaction rates across the Ag particle induce a torque that continuously reorients the microswimmers toward higher H_2O_2 concentrations, resulting in positive chemotaxis. The findings highlight the crucial role of particle morphology in chemotactic behavior and provide insights for designing artificial microswimmers with enhanced navigation capabilities in chemical gradients.

1. Introduction

Bio-hybrid robotics lies at the intersection of biology and robotics and promises to revolutionize advanced intelligent systems as an enabling technology in real-world applications such as biometric and biomedical devices, environmental monitoring, and soft robotics. To achieve this ambitious goal, we need to understand how far we can push the artificial components toward smarter behaviors and how to subsequently control them. Especially on the microscale the emerging properties resemble remarkably the intrinsic behaviors of living entities[1] which are relevant in biomedical terms.[2,3] In order to create smart and versatile

Z. Xiao, M. Voigtmann, J. Simmchen
Pure and Applied Chemistry
University of Strathclyde, UK and Chair of Physical Chemistry, TU Dresden
01069 Dresden, Germany
E-mail: juliane.simmchen@strath.ac.uk

J. Simmchen
Pure and Applied Chemistry
UoS, UK

The ORCID identification number(s) for the author(s) of this article can be found under https://doi.org/10.1002/aisy.202400839.

microscale tools, we need to explore how to influence and tune these synthetic behaviors.

One example that is often associated with living organisms locating nutrients, is chemotaxis, the phenomenon whereby an individual moves in the direction of a nonuniform distribution of a physical quantity, specifically movement up or down a gradient. This process is ubiquitous in living systems and has been shown to influence important processes ranging from inflammation,[4,5] neuronal patterning,[6] wound healing,[7] tumor spread in cancer,[8,9] and even embryogenesis.
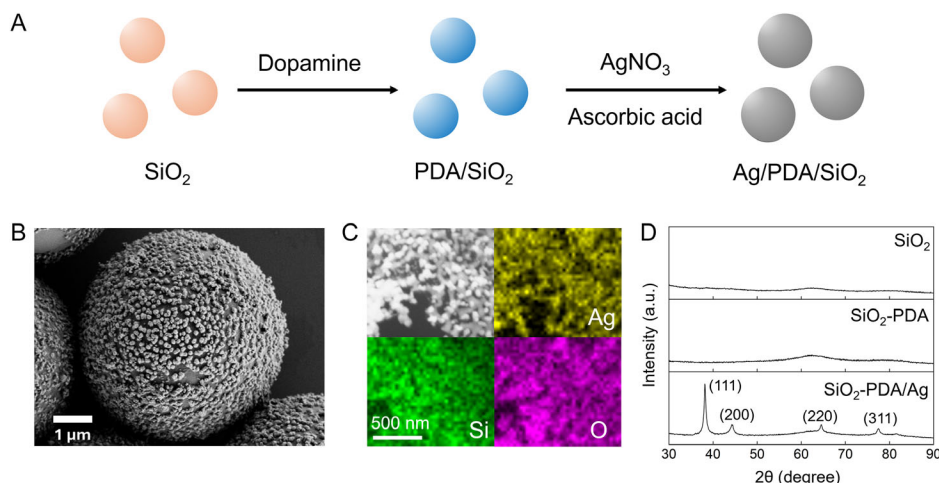
Artificial microswimmers are able to mimic natural tactic behaviors,[10,11] of special interest is chemotaxis even without complex sensing and signaling mechanisms.[12–18] Some chemically driven chemotactic micromotors have been reported, although they differ in their mechanisms. The basic principle is to reorient the swimmers in the direction of the gradient according to activity differences that induce torques.[19] Some recent literature presented orientation-driven chemotaxis.[20,21] Although different properties such as swimmer morphology and size ratio have been predicted to be crucial for the direction and characteristics of tactic behavior,[22] this influence has not yet been investigated.

Here, we report the shape-dependent chemotaxis of self-assembled doublet microswimmers with different morphologies. The tunable preparation of this type of active particle does not require complex material preparation and the obtained doublets show chemotactic behavior in a fuel gradient (H_2O_2). The catalytic activity on the Ag surface and the unique double-sphere structure of the microswimmer enable them to move autonomously in H_2O_2 with the Ag head forward. Note here that the peroxide degradation on a silver surface is not a perfectly catalytic process, but the silver is partially dissolved.[23] In the H_2O_2 gradient, the difference in the reaction rate across the Ag particle leads to a torque exerted on the swimmer, which constantly tunes the orientation of the doublets toward the high concentration of H_2O_2 and achieves the positive chemotaxis of them.

2. Result and Discussion

The Ag colloids are synthesized by reducing a layer of Ag on the 5 μm-sized silica (SiO_2) particles as schematically illustrated in **Figure 1**A according to a previously reported method.[24] In short,

ADVANCED
SCIENCE NEWS

www.advancedsciencenews.com

ADVANCED
INTELLIGENT
SYSTEMS
Open Access

www.advintellsyst.com

Figure 1. Synthesis of Ag-coated particles: A) Scheme of the process of Ag coating reaction. B) SEM micrograph of the Ag-coated particle. C) EDX-mapping of different elements of Ag, Si, and O. D) XRD patterns of the pure SiO₂ colloids before and after dopamine functionalization and after Ag coating.

dopamine is mixed with negatively charged SiO₂ particles, leading to the polymerization of dopamine on the SiO₂ surfaces, forming a continuous and adhesive poly-dopamine (PDA) layer. Subsequently, a AgNO₃ solution is added to the dopamine-coated SiO₂. The Ag ions adhere to the PDA layer and are then reduced by ascorbic acid, leading to the formation of a coherent Ag layer that covers the particle. The scanning electron microscopy (SEM) micrograph shown in Figure 1B illustrates that the synthesized Ag colloids have a regular, spheroidal morphology, and a uniform Ag coating. Given the relatively thin layer of Ag compared to the silica particles, the diameter of the Ag colloids remains close to 5 μm. The elemental distribution of Ag, Si, and O within the colloids is confirmed through energy-dispersive X-ray (EDX) spectroscopy, as demonstrated in Figure 1C, proving the

presence of Ag. Additionally, X-ray diffraction (XRD) analysis in Figure 1D reveals distinct signals corresponding to the Ag element after the coating procedure, further indicating the successful deposition of Ag on the colloids.

In the presence of hydrogen peroxide (H_2O_2), Ag colloids exhibit catalytic activity that attracts the surrounding SiO₂ particles toward them. The process is illustrated in **Figure 2**A as follows: Ag catalyzes the decomposition of H_2O_2, although less effective compared to platinum (Pt). The decomposition process involves the generation of reactive oxygen species, Ag ions, and hydroxide (OH^-) ions and the release of them into the solution. OH^- ions, with a diffusion coefficient of $5.27 \times 10^{-9} \, m^2 \, s^{-1}$, diffuse more rapidly than Ag ions, which have a diffusion coefficient of $1.65 \times 10^{-9} \, m^2 \, s^{-1}$. This difference in diffusivities
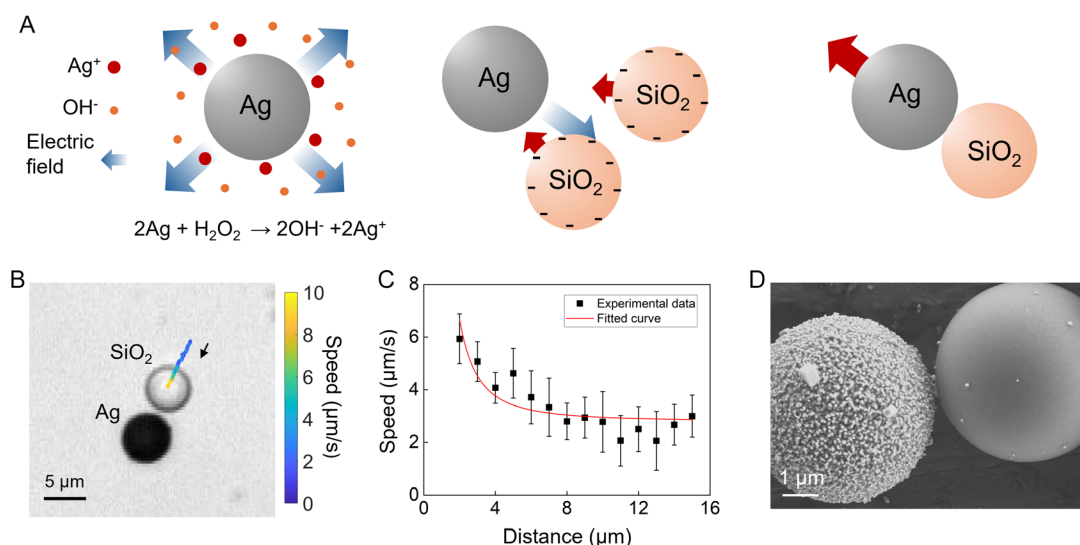

Figure 2. Formation of doublets: A) Schematic illustration of the formation of doublets. B) Micrograph showing a time lapse of the SiO₂ particles phoretically moving toward the Ag colloid. C) The averaged speeds of SiO₂ particles over distance showed an inverse correlation between them, from which we can infer a phoretic interaction between the Ag particles and SiO₂ particles. D) SEM micrograph showing a typical doublet in detail.

establishes an outward electric field pointing from Ag colloids that attract the negatively charged SiO_2 particles toward them. The simulated electric potential around the Ag particle, which was performed by a COMSOL implementation of a finite element method (FEM), is shown in Figure S4, Supporting Information, proving the outward direction of the electric field. Figure 2B shows a typical trajectory of a SiO_2 particle approaching an active Ag colloid in a H_2O_2 environment, showing an increase in the particle's velocity as it moves closer to the Ag colloid. A more quantitative analysis of these interactions was performed by measuring the speeds v of over 20 SiO_2 particles at various distances from the Ag colloid (Figure 2C). The resulting data were fitted with an $\frac{A}{r^2}$ relationship, where A is a fitting parameter and r is the particle–colloid separation. This scaling can be rationalized by considering that the ions concentration c generated by the Ag decreases as $1/r$, while the resulting electric field E, which drives the phoretic motion, is proportional to the Δc and thus scales as $1/r^2$.[25,26] Consequently, the particle velocity v, which is proportional to E, also scales as $1/r^2$. Once the particles are close enough together, the Van-der-Waals force between them becomes significant and permanently binds them together.[27] Figure 2D shows a typical SEM image of a doublet. These Ag-SiO_2 doublets exhibit high degrees of asymmetry, a characteristic that facilitates active motion[28] due to unbalanced flows around the doublets, driving the particles toward the Ag

sphere. In the experiment not only single Ag-SiO_2 doublets can result but also multi-particle structures due to the increased number of SiO_2 particles aggregating around a single Ag colloid (as shown in Figure S1, Supporting Information). By precise tuning of the concentration and ratio of Ag and SiO_2 particles, it is possible to control the extent of aggregation and suppress the formation of such multi-particle structures.

To understand the active dynamics of doublet particles, we first observe them in a homogeneous H_2O_2 environment. **Figure 3**A presents a time-lapse image capturing a doublet with its Ag head leading the movement, as shown in Video S2, Supporting Information. To analyze the mechanics of movement, we tracked changes in both the orientation angle and the direction angle of the doublets as they moved. Figure 3B illustrates the dynamic behavior of a doublet in a homogeneous H_2O_2 environment, specifically focusing on changes in its direction and orientation angles. The inset provides a schematic representation of these angles: the orientation angle denotes the direction in which the Ag head points during motion, while the direction angle corresponds to the instantaneous trajectory of the doublet. To quantify the relationship between these angles, we calculated the angular difference, $\Delta\theta$, for multiple particles and averaged the results. The analysis reveals that $\Delta\theta$ is minimal, indicating a strong alignment between the orientation of the Ag head and the direction of the doublet's movement. This suggests that
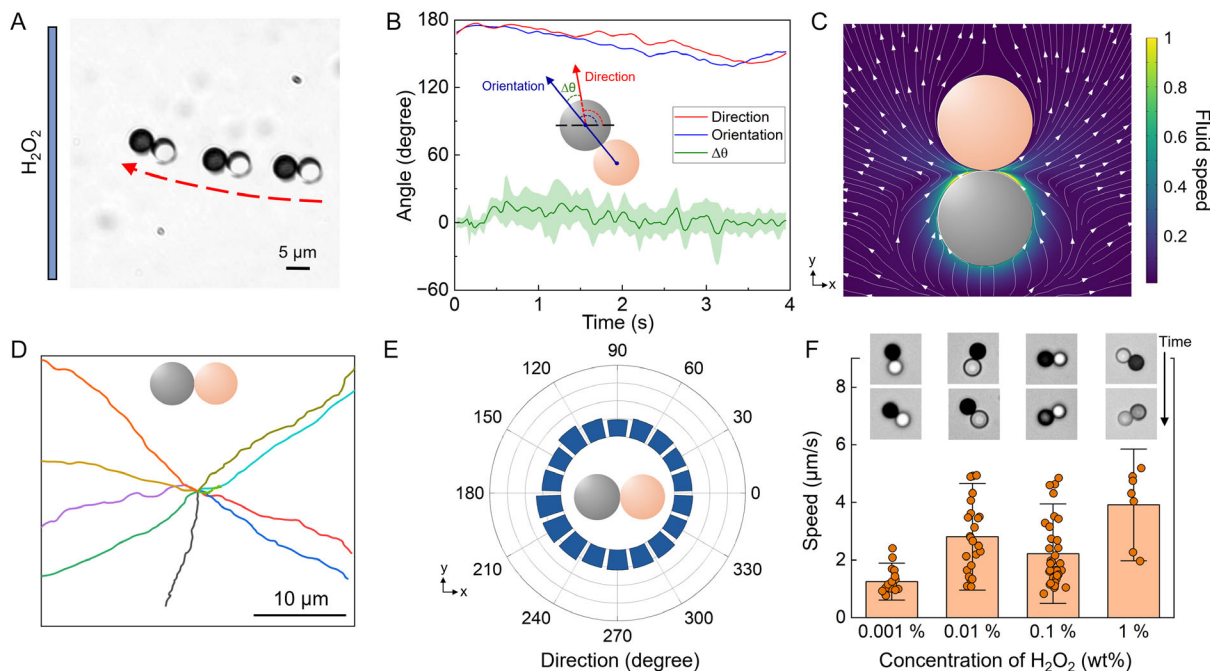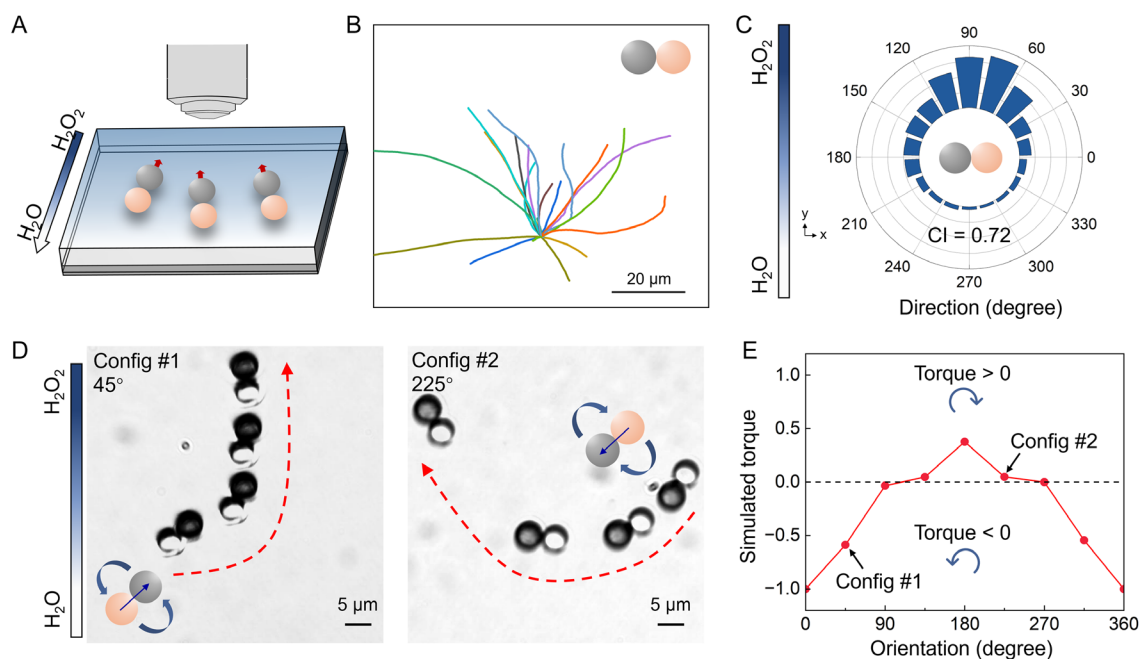

Figure 3. Characteristics and simulation of the motion of doublets in a homogeneous H_2O_2 environment. A) Time-lapse images of the motion of the doublet in a homogeneous H_2O_2 environment. B) Orientational and directional angle evolution of a doublet as a function of time during the motion. Inset: The blue arrow denotes the orientational vector of the doublet; the red arrow denotes the moving direction of the doublet; $\Delta\theta$ denotes the difference between the orientation and the direction. Shaded error bars indicate standard deviations of $\Delta\theta$ from doublets in (D). C) Simulated flow field around a doublet moving in H_2O_2. The white arrows denote the moving direction of the simulated flow. The color map represents the magnitude of the flow velocity. D) Tracking trajectories of motion of doublets in a homogeneous H_2O_2 environment. E) The distribution of the moving directions of the motion of doublets in (D). F) The speed of doublets at different H_2O_2 concentrations. The bar represents the average speeds, while the orange points indicate individual measurements. Error bars correspond to the standard deviation of the speed distribution. Representative micrographs (top) at each concentration show that at higher H_2O_2 concentrations, the Ag layer undergoes more pronounced degradation.

ADVANCED
SCIENCE NEWS

www.advancedsciencenews.com

ADVANCED
INTELLIGENT
SYSTEMS

Open Access

www.advintellsyst.com

the orientation of the Ag head predominantly decides the movement direction of the doublet. Notably, a slight drift was observed, which was more pronounced than that seen in corresponding Janus particles. In order to explore the mechanics of doublet motion further, we performed FEM simulations with the near-field components, modeling the electric potential and fluid flow of a fixed doublet in an H_2O_2 environment, see finite element simulations part for details. Figure 3C shows the simulated flow field around the doublet, which points from the Ag side to the SiO_2 side, confirming the Ag-leading direction of movement found experimentally. This is in agreement with previous experiments,[29,30] which reported a movement toward the catalytic hemisphere for Ag@SiO_2 Janus particles, which we also confirm (see Figure S5, Supporting Information). Figure 3D shows trajectories of doublets moving in H_2O_2. It reveals that the movement directions of the doublets are randomly distributed when in a homogeneous (non-gradient) environment. The trajectories are further analyzed by aggregating all the instantaneous moving directions, which are visually represented in a rose plot in Figure 3E. This plot indicates the absence of any preferred directions. We then investigate the dependence of H_2O_2 concentration on the activity of the doublets (Figure 3F). Although the overall trend shows that their speeds increase with the H_2O_2 concentration, we also observed a small drop at 0.1%. We suspect that this subtle decrease in speed may be related to the more pronounced degradation of the Ag layer at higher concentrations. As illustrated in the inset micrographs, with increasing H_2O_2 concentrations, the Ag particles, initially appearing dark, become lighter over time. This morphological evolution, coupled with enhanced catalytic

activity at higher concentrations, might explain the observed correlation between H_2O_2 concentration and doublet speed.

To observe the behavior of doublets in environments demonstrating chemotactic responses to fuel gradients, we employed our previously presented microfluidic setup designed to generate a gradient between water and H_2O_2 (**Figure** 4A).[18] This setup involves the co-flow of these substances, which is subsequently halted in a controlled manner to eliminate disturbances from fluid turbulence that could lead to intrinsic responses, as detailed in previous studies.[31,32] Initially, two parallel channels are loaded with H_2O_2 and water, respectively, and injected through a microfluidic chip. Upon stopping the flow, H_2O_2 diffuses from the fuel to the water channel, establishing a concentration gradient over time in the chip (see Figure S2, Supporting Information for a more detailed schematic illustration). We observed doublet movements within this H_2O_2 gradient but without any flow influence. Trajectory analysis, as shown in Figure 4B, reveals a predominant movement of doublets toward regions of higher H_2O_2 concentration, thereby indicating positive chemotaxis. This chemotactic behavior is quantitatively evaluated using the Chemotactic Index (CI), defined as the ratio of displacement toward the gradient relative to the total path length, with values ranging from +1 (indicative of positive chemotaxis) to −1 (representative of negative or anti-chemotaxis).[33] Our results, with a CI of 0.72, suggest a pronounced directional persistence in the chemotactic movement of the doublets. We use this parameter to facilitate comparison with different tactic systems, for example biological microswimmers like *E. coli* toward sugar gradients, which does not necessarily require either of the motion or taxis


Figure 4. Characteristic and simulation of the chemotaxis of doublets in a gradient of H_2O_2. A) Scheme of the setup of the chemotaxis experiment. B) Tracking trajectories of the chemotaxis of doublets in a gradient of H_2O_2. C) The distribution of the moving directions of the chemotaxis in (B). D) Time-lapse images of the reorientation process of doublets within a H_2O_2 gradient, with initial orientations of 45 and 225°, respectively. The insets indicate the direction of their rotational adjustments during the reorientation process. E) The calculated torques on doublets at different initial orientations. The negative torque values correspond to the counter-clockwise rotation of the doublet, while positive torque values represent clockwise rotation.

**ADVANCED
SCIENCE NEWS**

www.advancedsciencenews.com

**ADVANCED
INTELLIGENT
SYSTEMS**
Open Access

www.advintellsyst.com

strategies to be similar or comparable. Further analysis using a rose plot of instantaneous movement directions (Figure 4C) supports these findings, presenting a clear tendency of the doublets to migrate toward higher H_2O_2 concentrations.

To understand the mechanism underlying the observed positive chemotaxis of doublets in the H_2O_2 gradient, we analyzed closely their motion within the gradient, also complemented by FEM simulations. Figure 4D illustrates the alignment dynamics of doublets in two configurations under an H_2O_2 gradient. In configuration #1, the doublet initially exhibits a misalignment, with its orientation angle at 45°. Over time, the doublet undergoes counter-clockwise rotation, realigning its orientation toward the direction of higher H_2O_2 concentration (90°). This alignment process is pivotal, as the direction of motion is governed by the orientation of the head, leading to continuous navigation along the chemical gradient. In configuration #2, the initial orientation of the doublet is at 225°, resulting in a clockwise rotation also to 90°. Despite the opposite rotation modes, the doublets similarly adjust their orientations over time, ultimately aligning toward the direction of higher H_2O_2 concentration. These observations demonstrate the doublet's capacity to reorient and navigate effectively in response to chemical gradients, regardless of initial orientation. Crucially, these adjustments are driven not by biological sensory mechanisms but by the creation of mechanical torques resulting from asymmetric activities, which arise due to differential fuel (i.e., H_2O_2) availability at distinct positions on the doublet. (Note, the term force- and torque-free refers to the system of the particle and the thin layer).[19] To further investigate the relationship between torque and the initial orientation of the doublet, we conducted FEM simulations for various initial orientation angles ranging from 0 to 360°. For each angle, the torque exerted on the doublet was calculated and subsequently normalized to focus on the qualified trends (Figure 4E). As illustrated in the inset, a negative torque value corresponds to counterclockwise rotation, while a positive torque indicates clockwise rotation. The results reveal that at orientations of 90 and 270°, where the doublet faces directly along or opposite the gradient, the torque approaches zero, indicating no net rotation. However, for orientation angles less than 90° or greater than 270°, the torque is negative, resulting in a counterclockwise rotation. This rotation realigns the doublet toward regions of higher H_2O_2 concentration. Conversely, for orientation angles between 90 and 270°, the torque is positive, driving a clockwise rotation that also reorients the doublet toward the gradient. These findings strengthen the torque-driven mechanism by which the doublet adjusts its orientation to navigate effectively along the chemical gradient.

To further substantiate the proposed chemotactic mechanism, we examined the behavior of Ag@SiO₂ Janus particles and doublet particles with asymmetric structures (5–2 µm) in an H_2O_2 gradient. The time-lapsed micrographs are shown in Figure S5, Supporting Information. The trajectory data for the Ag@SiO₂ Janus particles, as illustrated in **Figure 5**A, exhibit biased motion similar to that of the symmetric structure (5–5 µm) doublet particles. The rose plot is presented in Figure 5B accordingly, with a CI of 0.69. However, the doublet particle with a pronounced asymmetry—a 5 µm Ag head paired with a 2 µm SiO₂ body—does not display clear chemotactic behavior, as evidenced in
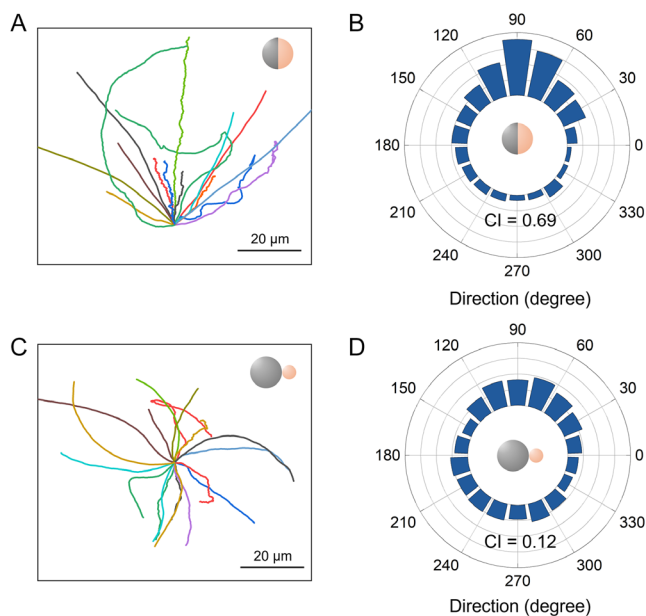
Figure 5. A) Tracking trajectories and B) corresponding distribution of movement directions for chemotaxis of Ag@SiO₂ Janus particles in a H_2O_2 gradient. C) Tracking trajectories and D) corresponding distribution of movement directions for chemotaxis of doublets with an asymmetric structure (5–2 µm) in a H_2O_2 gradient.

Figure 5C,D with a CI of 0.12. This observation leads us to hypothesize that effective chemotaxis is contingent upon a significant symmetry breaking which influences the flow dynamics around the particle. The smaller SiO₂ component, being only 2 µm in size, is insufficient to disrupt the symmetric flow pattern around the Ag particle, which is crucial for generating the directional torque needed for clear chemotactic movement. Thus, the lack of a marked asymmetry in this case results in an absence of pronounced chemotactic behavior.

3. Conclusion

We have successfully synthesized micrometer-sized doublet colloidal motors and demonstrated positive chemotaxis, which navigate along a chemical concentration gradient akin to natural chemotactic microorganisms. The unique Ag@SiO₂-SiO₂ doublet architecture of these motors facilitates their tactic motion toward a high concentration of H_2O_2. Detailed analysis reveals that these changes are driven by the dynamic alignment induced by the H_2O_2 gradient and the generated torque, which actively reorients the colloidal motors. The underlying mechanism involves the generation of an unbalanced local flow on the motor surface due to catalytic reactions, resulting in a net torque. This torque persistently guides the colloidal motors towards higher H_2O_2 concentrations, enabling positive chemotaxis. The FEM simulations and calculations corroborate this mechanism, providing a solid theoretical foundation for the observed behavior. Changing the morphology of the doublet to asymmetric sizes or even a normal Janus particle geometry changes the chemotactic index but not the overall phenomenon as predicted.[22] These doublet colloidal motors, with their pronounced

chemotactic capability, hold potential for advanced applications such as active targeted delivery. The local separation of propulsion and inert body allows for the integration of further bioinspired designs and functionalities and opens new avenues in the development of autonomously navigating microsystems.

4. Experimental Section

The silver particles are synthesized as follows: 5 μm SiO$_2$ particles (Sigma-Aldrich) were washed once with ethanol and twice with DI water. Subsequently, they were added to a solution of $2\,\text{g}\,\text{L}^{-1}$ dopamine in $10\,\text{mmol}\,\text{L}^{-1}$ Tris. The suspension was stirred for 30 min (the color changes to black, due to the oxidation of dopamine). Afterwards, the particles were washed with DI water, until the resulting supernatant was colorless. The PDA-covered particles were transferred to a $[\text{Ag}(\text{NH}_3)_2]^+\text{NO}_3^-$ solution and again stirred for 15 min. The $[\text{Ag}(\text{NH}_3)_2]^+\text{NO}_3^-$ solution was prepared previously by adding 25% NH$_3$ solution to a 10 g/L solution of AgNO$_3$ until the immediate precipitated AgOH was completely dissolved again. In the next step, the particles were washed twice and suspended in 2.5 mL water. The suspension was transferred to 5 mL of a $10\,\text{g}\,\text{L}^{-1}$ solution of ascorbic acid, to reduce the silver cations on the particles. After stirring for 1 min, the particles were washed again three times with DI water.

For the characterization of silver particles, 3 μL of a particle dispersion was placed on an aluminum tap and then allowed to dry. SEM and EDX measurements were carried out on a Zeiss Gemini SEM 300 instrument with Ultim Max 65 detector from Oxford Instruments Nanoanalysis at an accelerating voltage of 10 keV. Analyses and graphic representation of the data was done using AZtec software from Oxford Instruments. SEM images showed a uniform coating of silver on the SiO$_2$ particles, EDX clearly distinguished the Ag element from other substances, and XRD proved the existence of Ag on the particles.

Motion experiments were performed using Ag particles and SiO$_2$ which were dispersed to 0.001 wt% in DI water before use. 10 μL Ag particles solution and 10 μL SiO$_2$ particles solution were added to a plasma-cleaned glass slide, respectively. Then a specific amount and concentration of H$_2$O$_2$ solution was added to the particle mixture. The formation and movement of the doublets were captured and recorded under an inverted microscope.

Chemotaxis experiments were conducted in a feedback loop system.[18] The gradient was generated in a microfluidic set-up, with the microfluidic cell mounted on a microscope. To ensure the formation of a stable gradient, the cell was flushed for at least 1 min with water and 1% H$_2$O$_2$ through the respective channels. Subsequently, the particles were added through the water channel. To observe movement in the gradient, the flow was stopped by applying equal pressures at the inlet and outlet channels. Then the chemotaxis of the doublets was observed in a linear H$_2$O$_2$ gradient without any turbulence of flow. The motion of the chemotaxis was captured and recorded under an upright microscope.

Data analysis of the motion videos were analyzed by MATLAB software to extract the coordinates of the particle.

The instantaneous speeds are calculated as follows:

$$v = \sqrt{(x_{i+1} - x_i)^2 + (y_{i+1} - y_i)^2}/\delta t \tag{1}$$

where x_i and y_i are the x and y coordinates of the particle at the previous frame, while x_{i+1} and y_{i+1} are the x and y coordinates of the particle at the next frame, δt is the time of one frame.

The moving directions of the doublet is calculated as follows

$$\theta_{\text{direction}} = \arctan\frac{y_{i+1} - y_i}{x_{i+1} - x_i} \tag{2}$$

The orientations of the doublet is calculated as follows

$$\theta_{\text{orientation}} = \arctan\frac{y_{\text{Ag}} - y_{\text{SiO}_2}}{x_{\text{Ag}} - x_{\text{SiO}_2}} \tag{3}$$

where x_{Ag} and y_{Ag} are the x and y coordinates of the center of the Ag particle, while $x\text{SiO}_2$ and $y\text{SiO}_2$ are the x and y coordinates of the center of the particle.

Finite element simulations: to simulate the motion and the chemotaxis of doublets in H$_2$O$_2$, we constructed a 3D COMSOL model where two spheres, each 5 μm in diameter, are placed at the center of a cubic box with sides measuring 100 μm (see Figure S3, Supporting Information). One sphere is designated as an active Ag particle, while the other is a passive SiO$_2$ particle. The cube serves as the computational domain and is filled with water. The electric potential and fluid flow within the domain are solved using a nonlinear steady-state solver implemented in COMSOL. Based on previous work,[30] we assume an ionic diffusiophoresis mechanism for the doublets. The electrochemical decomposition of H$_2$O$_2$ to Ag$^+$ and OH$^-$ occurs on the surface of the Ag particle.

Two modules in COMSOL were used here: electrostatics and creeping flow. In the electrostatics module, the computational domain is governed by the following Equation (4)

$$E = -\nabla V \tag{4}$$

where E is the electric field and V is the electric potential. The electric field is further determined by the space charge density at each point in the domain (5)

$$\nabla \times (\varepsilon E) = \rho_v \tag{5}$$

where ε is the medium's electrical permittivity, and ρ_v is the space charge density.

The doublet in our model produces Ag$^+$ and OH$^-$ ions at a flux of J only at the Ag surface, whereas the SiO$_2$ sphere is chemically inert. The electrical double layer (EDL) of the doublet is assumed to be infinitely thin here. According to the literature,[34] the Ag face with a flux J carries an extrinsic surface charge density ρ_s given by (6)

$$\rho_s = \varepsilon E = \varepsilon \frac{J K_B T}{2 e n_0}(1/D_+ - 1/D_-) \tag{6}$$

where ε is the medium electrical permittivity, E is the electric field intensity, K_B is the Boltzmann constant, T is the temperature, e is the elementary charge, n_0 is the bulk ionic concentration, and $1/D_+$ and $1/D_-$ are the diffusion coefficients of Ag$^+$ and OH$^-$.

On the SiO$_2$ surface

$$\rho_s = 0 \tag{7}$$

For a doublet moving in a uniform H$_2$O$_2$ bulk solution, J is constant across the doublet surface. As the doublet placed in H$_2$O$_2$ with a linear gradient distribution, J is derived as the following Equation (8)

$$J = \nabla J_0 \times R \cos\theta \tag{8}$$

where J_0 is the maximum flux on the Ag surface, R is the radius of the doublet, and θ is the angle between the orientation of the doublet and the H$_2$O$_2$ gradient direction.

In the creeping flow module, the computational domain is governed by the following equation

$$\nabla \times u = 0 \tag{9}$$

$$\nabla p = \eta \nabla^2 u \tag{10}$$

where p is the pressure, η is the dynamic viscosity of water, and u is the fluid flow velocity.

The two modules are coupled through an electroosmotic boundary condition on the particle surfaces

$$U_{\text{eo}} = \frac{\zeta \varepsilon}{\eta} E_{\text{tan}} \tag{11}$$

where U_{eo} is the electroosmotic velocity on the particle surface, ζ is the zeta potential (SiO$_2$ surface set to be -40 mV, Ag surface set to be

-29 mV according to measurements), and E_{tan} is the tangential component of the electric field that is solved by the (4) and (5).

The torque exerted by the electroosmotic flow on the doublet is calculated as follows

$$M = F_N R \qquad (12)$$

where F_N is the force exerted by the flow, decomposed tangentially to the surface, R is the radius of the doublet, and M is the torque. The positive value of M denotes a clockwise rotation of the doublet, while the negative value denotes an anti-clockwise rotation.

Supporting Information

Supporting Information is available from the Wiley Online Library or from the author.

Conflict of Interest

The authors declare no conflict of interest.

Author Contributions

Zuyao Xiao: investigation (lead); methodology (lead); software (lead); validation (equal); visualization (lead); writing—original draft (lead). **Maximilian Voigtmann**: investigation (equal); methodology (equal); writing—original draft (supporting). **Juliane Simmchen**: conceptualization (lead); formal analysis (supporting); funding acquisition (lead); supervision (lead); validation (supporting); writing—original draft (supporting); writing—review and editing (lead).

Data Availability Statement

The data that support the findings of this study are available from the corresponding author upon reasonable request.

[1] A. Nsamela, A. I. Garcia Zintzun, T. D. Montenegro-Johnson, J. Simmchen, *Small* **2023**, *19*, 2202685.

[2] Y. Feng, Y. Yuan, J. Wan, C. Yang, X. Hao, Z. Gao, M. Luo, J. Guan, *Appl. Phys. Rev.* **2021**, *8*, 1.

[3] J. Lin, C. Lian, L. Xu, Z. Li, Q. Guan, W. Wei, H. Dai, J. Guan, *Adv. Funct. Mater.* **2024**, 2417146.

[4] C. H. Wong, B. Heit, P. Kubes, *Cardiovasc. Res.* **2010**, *86*, 183.

[5] K. S. Johnson, K. M. Ottemann, *Curr. Opin. Microbiol.* **2018**, *41*, 51.

[6] L. Luo, Q. Wen, J. Ren, M. Hendricks, M. Gershow, Y. Qin, J. Greenwood, E. R. Soucy, M. Klein, H. K. Smith-Parker, A. C. Calvo, D. A. Colon-Ramos, A. D. T. Samuel Y. Zhang, *Neuron* **2014**, *82*, 1115.

[7] J. A. van Diepen, J. H. Robben, G. J. Hooiveld, C. Carmone, M. Alsady, L. Boutens, M. Bekkenkamp-Grovenstein, A. Hijmans, U. F. Engelke, R. A. Wevers, M. G. Netea, C. J. Tack, R. Stienstra, P. M. T. Deen, *Diabetologia* **2017**, *60*, 1304.

[8] E. T. Roussos, J. S. Condeelis, A. Patsialou, *Nat. Rev. Cancer* **2011**, *11*, 573.

[9] A. Puliafito, A. De Simone, G. Seano, P. A. Gagliardi, L. Di Blasio, F. Chianale, A. Gamba, L. Primo, A. Celani, *Sci. Rep.* **2015**, *5*, 15205.

[10] T. Bickel, G. Zecua, A. Würger, *Phys. Rev. E* **2014**, *89*, 050303.

[11] S. Auschra, A. Bregulla, K. Kroy, F. Cichos, *Eur. Phys. J. E* **2021**, *44*, 90.

[12] Y. Hong, N. M. Blackman, N. D. Kopp, A. Sen, D. Velegol, *Phys. Rev. Lett.* **2007**, *99*, 178103.

[13] L. Baraban, S. M. Harazim, S. Sanchez, O. G. Schmidt, *Angew. Chem.* **2013**, *52*, 21.

[14] K. K. Dey, S. Bhandari, D. Bandyopadhyay, S. Basu, A. Chattopadhyay, *Small* **2013**, *9*, 1916.

[15] C. Jin, C. Krüger, C. C. Maass, *Proc. Natl. Acad. Sci. U.S.A.* **2017**, *114*, 5089.

[16] A. Joseph, C. Contini, D. Cecchin, S. Nyberg, L. Ruiz-Perez, J. Gaitzsch, G. Fullstone, X. Tian, J. Azizi, J. Preston, G. Volpe, G. Battaglia, *Sci. Adv.* **2017**, *3*, e1700362.

[17] F. Peng, Y. Tu, J. C. Van Hest, D. A. Wilson, *Angew. Chem. Int. Ed.* **2015**, *54*, 11662.

[18] Z. Xiao, A. Nsamela, B. Garlan, J. Simmchen, *Angew. Chem. Int. Ed.* **2022**, *61*, e202117768.

[19] M. N. Popescu, W. E. Uspal, C. Bechinger, P. Fischer, *Nano Lett.* **2018**, *18*, 5345.

[20] F. Mou, Q. Xie, J. Liu, S. Che, L. Bahmane, M. You, J. Guan, *Nat. Sci. Rev.* **2021**, *8*, nwab066.

[21] C. Zhou, C. Gao, Y. Wu, T. Si, M. Yang, Q. He, *Angew. Chem. Int. Ed.* **2022**, *61*, e202116013.

[22] H. D. Vuijk, H. Merlitz, M. Lang, A. Sharma, J.-U. Sommer, *Phys. Rev. Lett.* **2021**, *126*, 208102.

[23] C. Zhou, H. Zhang, J. Tang, W. Wang, *Langmuir* **2018**, *34*, 3289.

[24] W. Wang, Y. Jiang, Y. Liao, M. Tian, H. Zou, L. Zhang, *J. Colloid Interface Sci.* **2011**, *358*, 567.

[25] D. Prieve, J. Anderson, J. Ebel, M. Lowell, *J. Fluid Mech.* **1984**, *148*, 247.

[26] R. Golestanian, T. Liverpool, A. Ajdari, *New J. Phys.* **2007**, *9*, 126.

[27] D. Velegol, in *Colloidal Systems*, Wild Scholars Media, US **2016**.

[28] F. Schmidt, B. Liebchen, H. Löwen, G. Volpe, *J. Chem. Phys.* **2019**, *150*, 9.

[29] P. Chattopadhyay, J. Simmchen, *ChemRxiv*, **2019**, https://doi.org/10.26434/chemrxiv.9391925.v1.

[30] Z. H. Shah, S. Wang, L. Xian, X. Zhou, Y. Chen, G. Lin, Y. Gao, *Chem. Commun.* **2020**, *56*, 15301.

[31] J. Katuri, W. E. Uspal, J. Simmchen, A. Miguel-López, S. Sánchez, *Sci. Adv.* **2018**, *4*, eaao1755.

[32] P. Sharan, Z. Xiao, V. Mancuso, W. E. Uspal, J. Simmchen, *ACS nano* **2022**, *16*, 4599.

[33] J. Varennes, H.-R. Moon, S. Saha, A. Mugler, B. Han, *PLoS Comput. Biol.* **2019**, *15*, e1006961.

[34] T. R. Kline, J. Iwata, P. E. Lammert, T. E. Mallouk, A. Sen, D. Velegol, *J. Phys. Chem. B* **2006**, *110*, 24513.